OPEN ACCESS

PEFC Electrocatalysts Supported on Nb-SnO_2 for MEAs with High Activity and Durability: Part II. Application of Bimetallic Pt-Alloy Catalysts

PEFC Electrocatalysts Supported on Nb-SnO_2 for MEAs with High Activity and Durability: Part II. Application of Bimetallic Pt-Alloy Catalysts

S. Matsumoto,[1] M. Nagamine,[1] Z. Noda,[1,2] J. Matsuda,[3] S. M. Lyth,[3,4] A. Hayashi,[1,2,3,4,5,6,*] and K. Sasaki [1,2,3,4,5,6,*,z]

[1] *Department of Hydrogen Energy Systems, Faculty of Engineering, Kyushu University, Nishi-ku, Fukuoka 819-0395, Japan*
[2] *International Research Center for Hydrogen Energy, Kyushu University, Nishi-ku, Fukuoka 819-0395, Japan*
[3] *International Institute for Carbon-Neutral Energy Research (WPI-I2CNER), Kyushu University, Nishi-ku, Fukuoka 819-0395, Japan*
[4] *Platform of Inter / Transdisciplinary Energy Research (Q-PIT), Kyushu University, Nishi-ku, Fukuoka 819-0395, Japan*
[5] *Next-Generation Fuel Cell Research Center (NEXT-FC), Kyushu University, Nishi-ku, Fukuoka 819-0395, Japan*
[6] *Center for Co-Evolutional Social Systems, Kyushu University, Nishi-ku, Fukuoka 819-0395, Japan*

Bimetallic Pt-alloys supported on niobium-doped tin oxide (Nb-SnO_2) with a vapor-grown carbon fiber (VGCF) backbone are presented as electrocatalysts for polymer electrolyte membrane fuel cells (PEFCs). These can simultaneously achieve both high catalytic activity and high cycling durability for the oxygen reduction reaction (ORR). This was confirmed both in half-cell and full-cell membrane electrode assembly (MEA) configuration, using 60,000 start-stop potential cycles and 400,000 load potential cycles. In this study, we focus on alloying Pt with Co or Ni, and the best performance is achieved for Pt_3Co/Nb-SnO_2/VGCF electrocatalysts. The catalyst particles are selectively decorated on the Nb-SnO_2, resulting in improved resistance to carbon corrosion. Pt_3Co alloying was verified by FE-SEM and high-resolution STEM-EDS. High initial mass activity of 274 A g^{-1} at 0.9 V_{RHE} and 1840 A g^{-1} at 0.85 V_{RHE} was achieved, with enhanced durability compared to conventional Pt/C electrocatalysts.
 [DOI: 10.1149/2.0321814jes]

Manuscript submitted April 13, 2018; revised manuscript received October 8, 2018. Published October 23, 2018. This was Paper 1581 presented at the National Harbor, Maryland Meeting of the Society, October 1–5, 2017.

Polymer electrolyte membrane fuel cells (PEFCs) have been developed and commercialized worldwide as power sources for commercial automotive (e.g. private cars, forklifts, buses, and trucks), portable, and stationary applications.[1,2] Pt-decorated carbon black (Pt/C) is widely used as the electrocatalyst in PEFCs.[2–5] Carbon black has high electronic conductivity and surface area, which are important features for electrocatalyst supports. However, the cathode potential increases to ∼1.5 V vs. the reversible hydrogen electrode (RHE) upon start-stop cycling.[3] At this high potential, carbon is thermochemically unstable, and can be electrochemically oxidized leading to carbon corrosion, electrocatalyst layer thinning, and Pt nanoparticle detachment/aggregation. Therefore, conventional Pt/C electrocatalysts can suffer from poor voltage cycling durability.[3–5] One promising method to avoid this is to develop a catalyst support material which is stable against oxidative corrosion, even at a high potential.

As described in Part I of this study,[6] intensive research has been conducted to develop alternative support materials to carbon black, with high stability and electronic conductivity. One approach is to make carbon-based materials more stable by e.g. graphitization. For example, Wang et al.[7] reported that Pt-decorated carbon nanotubes (CNTs) with highly graphitic surface had improved stability compared to conventional Pt/C. The use of graphitized carbon black (GCB) catalyst supports can also lead to improved electrocatalytic stability.[8] Metal oxide supports have also been explored - since they cannot be further oxidized they are resistant to oxidative degradation.[8–20] Since the Nafion ionomer used in PEFCs is strongly acidic, electrocatalysts should be stable in strongly acidic environments at ∼80°C. In such severe conditions, the number of stable oxides is limited to materials such as SnO_2, TiO_2, Nb_2O_5, Ta_2O_5, and WO_3.[13–20] SnO_2 is well known as a semiconducting oxide with a relatively-high electronic conductivity among these oxides. One typical hypervalent donor for SnO_2, Sb^{5+}, is soluble under strongly-acidic PEFC conditions, as thermochemically expected[13] and experimentally verified.[21] In contrast, Nb_2O_5 is thermochemically stable under such strongly-acidic PEFC conditions,[13] also verified experimentally,[22] and the hypervalent Nb^{5+} dopant can also act as a donor for SnO_2.[15] While a significant increase in electronic conductivity would not be expected for inhomogeneous Nb^{5+} doping,[23] Nb-doped SnO_2 is an optimal combination of dopant and matrix oxide from both the stability and electronic conductivity viewpoints.[13–15] Studies of electrocatalysts supported on SnO_2 are receiving increased attention.[13–20] Power generation from MEAs applying such electrocatalysts has already been demonstrated.[14–16] However, despite being able to increase the electronic conductivity of semiconducting oxides by doping with e.g. Nb^{5+}, the conductivity is still insufficient compared to carbon-based supports.

Attempts have therefore been made to separate the functions of catalyst dispersion and electronic transport. In such catalyst systems, graphitized carbon is used as a filler with high electronic conductivity, whilst the platinum nanoparticles are selectively decorated on an oxide support, such as SnO_2. Such nanocomposite electrocatalysts can exhibit high potential cycling durability, since the Pt nanoparticles have no direct contact with the carbon backbone, thus preventing electrochemical carbon corrosion. For example, Horiguchi et al.[20] developed Pt-decorated nanocomposites of SnO_2 and carbon fibers, achieving reasonable electrochemical activity, and high potential cycling durability. In Part I of this study,[6] Pt-decorated Nb-SnO_2 catalyst supports on various types of conductive carbon fillers were examined. It has been demonstrated that Pt-decorated SnO_2-supported electrocatalysts deposited on conductive fillers can realize high catalytic activity, sufficient electrochemical characteristics, excellent start-stop cycle durability, and sufficient load cycle durability. However, in addition to the electronic conductivity improvement considered in the previous study,[6] further improvement especially in their catalytic activity is still desired.

One approach to further improve the catalytic activity is to prepare bimetallic Pt-based alloy catalysts, instead of a pure Pt catalyst. Here,

*Electrochemical Society Member.
[z]E-mail: sasaki@mech.kyushu-u.ac.jp

we focus on improvement of the catalytic activity by preparing Pt_xM_y (M = Co or Ni) bimetallic nanoparticles. Co and Ni are relatively stable metals in PEFC operating environment, and Pt_xM_y alloy catalysts are well known to be capable of exhibiting higher ORR activity than pure Pt catalysts.[24–39] In 1993, Mukerjee and Srinivasan[24] showed a two- to threefold enhancement of the electrocatalytic ORR activity of bimetallic Pt_3Ni, Pt_3Cr, and Pt_3Co alloy catalysts on carbon supports, attributed to lattice contraction of the alloys. Toda et al.[25,26] developed several kinds of Pt-based alloy catalysts, and their compositions and crystal structures were characterized. Their analysis of the ORR activity revealed that Pt-Co and Pt-Ni alloy catalysts exhibited 10 to 20 times higher mass activity than that of a pure Pt catalyst in the optimum composition. In addition, Tada et al.[26] and Stassi et al.[31] reported higher MEA I-V characteristics using Pt-Co cathode catalysts. Considerable increase in the ORR activity has been reported e.g. by Stamenkovic et al.[32] for $Pt_3Ni(111)$, Wu et al.[33] for truncated octahedral Pt_3Ni, and by Han et al.[34] for de-alloyed Pt-Ni nanoparticles. Catalytic activity of such Pt-alloys has been comprehensively reviewed by Gasteiger et al.,[35] Stamenkovic et al.,[36] Thompsett,[37] Debe,[38] and Stephens et al.[39] Recently, studies on ternary alloy electrocatalysts have also been conducted, achieving high initial ORR activity.[40–42]

So far, studies of Pt-alloy electrocatalysts have mainly been performed for carbon-based catalyst supports. No comprehensive studies of Pt-alloy catalysts have been made for oxide-supported electrocatalysts, especially including the preparation of Pt-alloy electrocatalysts, MEA fabrication, I-V characteristics, separation of the overvoltages, start-stop cycle durability, load cycle durability, and analysis of their nanostructure. In particular, the start-stop cycle durability up to 1.5 V is an important issue for studying bimetallic catalysts on metal oxide supports with carbon fillers. Durability against 60,000 start-stop cycles is equivalent to the lifetime of a fuel cell vehicle (FCV), and recommended evaluation protocols have been proposed by both the Fuel Cell Commercialization Conference of Japan (FCCJ)[43] and the New Energy and Industrial Technology Development Organization (NEDO).[44]

For FCV applications, it is also necessary to confirm the load cycling durability. The fluctuation in potential caused by acceleration and deceleration of FCVs is often evaluated as voltage cycle durability in the potential range between 0.6 and 1.0 V.[43,44] It has been reported that when Pt alloy electrocatalysts are applied, load cycle durability can suffer due to dissolution of the alloyed metal in addition to Pt dissolution.[45–47] This deterioration may originate from the Pt-alloy rather than the catalyst support, but experimental evaluation has not yet been conducted on the deterioration behavior of Pt-alloy catalysts on oxide supports. In considering their applicability to FCVs, it is essential to systematically evaluate not only ORR activity and electrochemical characteristics but also start-stop cycle durability and load cycle durability both in half-cell and full-cell MEA conditions.

Here, the aim is to develop Pt_xM_y bimetallic electrocatalysts on oxide supports, with the target of improving the catalytic activity. First, the preparation procedures of Pt-alloy electrocatalysts are examined and developed by varying the preparation conditions. In particular, the optimization of the heat-treatment temperature is critical in forming bimetallic alloys, whilst simultaneously preventing the formation of Pt-Sn alloys. After verifying homogeneous decoration of Pt-alloy nanoparticles on the oxide supports, the electrochemical surface area (ECSA) and ORR activity of the alloy catalysts are examined for Pt-Co and Pt-Ni bimetallic electrocatalysts with different chemical compositions and heat-treatment temperatures. The durability of these electrocatalysts and their MEAs is then analyzed by measuring the ECSA, I-V characteristics, overvoltages, and durability, by applying potential cycling simulating start-stop cycles and load cycles of FCVs.

Experimental

Preparation of support materials.—Vapor grown carbon fibers (VGCF-H, Showa Denko, Japan), which have high electronic conductivity[6] (e.g. a single fiber specific resistivity of 1×10^{-4} Ωcm[48]), were used as the conductive carbon filler in this study. First, niobium-doped tin oxide (Nb-SnO_2) was synthesized on the surface of VGCF via the ammonia co-precipitation method, as shown schematically in Figure 1a. The concentration of Nb in the SnO_2 was fixed at 2 mol% ($Sn_{0.98}Nb_{0.02}O_2$), as this has already been reported to show the highest electronic conductivity.[15] $SnCl_2 \cdot 2H_2O$ and $NbCl_5$ were added to an ethanol dispersion of VGCF, and diluted NH_3 solution was then added to this dispersion at a rate of 5 cc/min, followed by filtration and air-drying at 100°C for 10 h. The resulting powders were then heat-treated under flowing N_2 at 600°C for 2 h after dry-milling. The amount of Nb-SnO_2 loaded onto the VGCF was set to be 50 wt% which results in good coverage of metal oxide on the VGCF fibers, with high specific surface area, but without aggregation of the SnO_2.

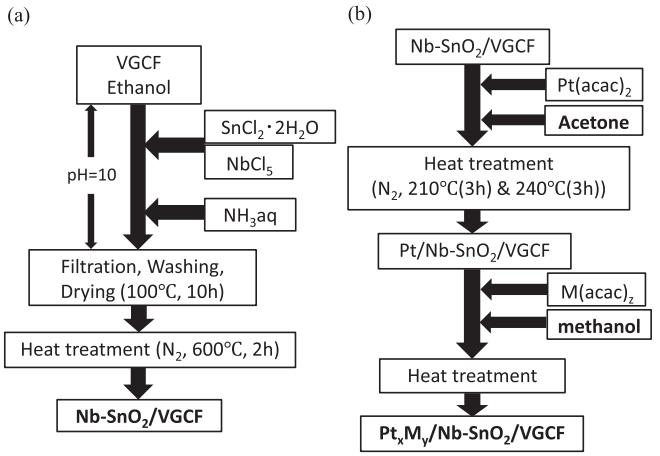

Figure 1. (a) Ammonia co-precipitation method and (b) acetylacetonate (acac) complex method.

Preparation of electrocatalysts.—Co-deposition of Pt and M (M = Co or Ni) was performed using a two-step platinum acetylacetonate (Pt(acac)$_2$) complex method.[49] Pt(acac)$_2$ can be dissolved in acetone, and Co(acac)$_2$ and Ni(acac)$_2$ can be dissolved in methanol. However, co-evaporation of the different solvents was difficult due to the difference in boiling point of acetone and methanol. Therefore, a two-step decoration protocol was applied. Figure 1b shows the procedure for Pt-alloy catalysts. First, the Nb-SnO_2/VGCF powder and Pt(acac)$_2$ were dispersed/dissolved in acetone via ultrasonication, and then the solvent was removed using rotary evaporator under reduced pressure. The resulting powder was then heat-treated under flowing N_2 at 210°C for 3 h, and then at 240°C for 3 h to form Pt/Nb-SnO_2/VGCF. In the case of the bimetallic Pt_xM_y alloy catalysts, Pt/Nb-SnO_2/VGCF and Co(acac)$_2$ or Ni(acac)$_2$ was dispersed/dissolved in methanol, ultrasonicated, and dried using rotary evaporator under reduced pressure. The heat-treatment conditions were varied in order to achieve Pt_xM_y alloying without reducing the SnO_2 to Sn metal. The Pt/M ratio was also varied to form Pt_xM_y/Nb-SnO_2/VGCF electrocatalysts. Additionally, for the Pt_xM_y/Nb-SnO_2/VGCF electrocatalysts, acid treatment was performed in 1 M HNO_3 at 80°C for 2 h before MEA preparation, in order to remove excess Co or Ni.

Characterization of electrocatalysts.—The microstructure and chemical composition of the prepared electrocatalysts were observed using a field-emission scanning electron microscope (FE-SEM, S-5200, Hitachi High-Technologies) and a high-resolution scanning transmission electron microscope (STEM, JEM-ARM200F, JEOL), with energy dispersive X-ray spectroscopy (STEM-EDS). The Nb-SnO_2 loading on VGCF was quantified using thermogravimetry (TG, Thermo plus EVO2, Rigaku). The atomic ratio and Pt and M loading on Nb-SnO_2/VGCF were measured using inductively-coupled plasma atomic emission spectrometry (ICP-AES, Shimadzu Corp., ICPE-9000).

Half-cell measurements were made to evaluate electrochemical activities of the obtained electrocatalysts. Each electrocatalyst was dispersed onto the Au disk of a working electrode (0.196 cm^2), with a loading of 17.3 $\mu g_{\text{-Pt}}$ cm^{-2}.[50] The counter electrode was a Pt wire, and the reference electrode was Ag/AgCl saturated in KCl. Cyclic voltammetry (CV) measurements were performed at a scanning rate of 50 mV s^{-1} in N_2-saturated 0.1 M $HClO_4$ solution, at 25°C. Pretreatments were carried out by potential cycling, in order to clean the catalyst surfaces. The potential range for pretreatments was 0.05 - 1.2 V_{RHE} for pure Pt catalysts, and 0.5 - 1.0 V_{RHE} for the bimetallic Pt_xM_y catalysts.[51] 50 pretreatment cycles were applied for the pure Pt catalysts, and 200 pretreatment cycles were applied for the bimetallic Pt_xM_y catalysts. After this, the electrochemical surface area (ECSA) of Pt was determined from the peak area in the hydrogen desorption region (0.05 - 0.4 V_{RHE}) obtained from the CV measurements. ORR activity was characterized by measuring the kinetic current determined from rotating disk electrode (RDE) measurements. The rotating speed of the electrode was set at various rates ranging from 2,500 to 400 rpm, and the potential was swept from 0.2 to 1.2 V_{RHE} at a scanning rate of 10 mV s^{-1} at 25°C. Mass activity (j_m) per unit Pt mass at 0.9 V_{RHE} and 0.85 V_{RHE} was derived to evaluate the ORR activities of the electrocatalysts.

The degradation of the electrocatalysts was evaluated according to procedures recommended by the FCCJ.[43] Potential cycles were applied simulating start-stop cycles and load cycles (in half-cell tests). Start-stop cycles tend to promote carbon corrosion - a triangular potential waveform was used between 1.0 and 1.5 V_{RHE} with 2 seconds per cycle, and the ECSA and mass activity after 60,000 cycles were measured. Meanwhile, load cycling tends to promote Pt dissolution - a rectangular potential waveform was used between 0.6 and 1.0 V_{RHE} with 6 seconds per cycle for 400,000 cycles, after which the ECSA and ORR were measured.

Preparation of MEAs.—Pt_3Co/Nb-SnO_2/VGCF or conventional Pt/C (TEC10E50E, 46.4 wt%-Pt, Tanaka Kikinzoku Kogyo Corp., Japan), 99.5% ethanol, ultra-pure water, and 5% Nafion solution, were well-dispersed using an ultrasonic homogenizer (UH-600, SMT Co., Ltd, Japan). The resulting electrocatalyst paste was then printed onto an electrolyte membrane (Nafion 212), using a spray printing system (C-3 J, Nordson). The electrode area was 1.0 cm^2 (1 cm × 1 cm). Pt/C was used for the anode, and Pt_3Co/Nb-SnO_2/VGCF was used for the cathode. The Pt loading was fixed as 0.3 $mg_{\text{-Pt}}$ cm^{-2} in each case for Pt and Pt-alloys. After spray printing, the electrode-printed membrane was hot-pressed at 132°C and 0.3 kN for 180 seconds. Finally, the Nafion membrane with attached electrocatalyst layers was sandwiched by gas diffusion layers (GDL). Teflon-coated carbon paper (Electrochem, EC-TP1-060T) without a microporous layer (MPL) was used for the anode, and Teflon-coated carbon paper (SGL Carbon, 25BC) with an MPL was used for the cathode.

Characterization of MEAs.—The I-V characteristics of MEAs were evaluated using a cell holder recommended by NEDO.[52] Measurements were performed at a cell temperature and gas humidification temperature of 80°C, and 100% relative humidity (RH). The gas utilization of H_2 and air was set to be 2% for both the cathode and the anode. MEAs were pre-treated at 0.5 V for 5 h before the actual I-V measurements. As well as the I-V curves, the ohmic resistance was measured using an AC impedance analyzer (1255B, Solatron), and IR losses were separated. Using the IR-free voltage, the activation overvoltage and the concentration overvoltage were further separated based on Tafel plots in the low current density region. The difference between the voltage defined by the Tafel slope and the theoretical open circuit voltage (OCV) was described as the activation overvoltage. Then, the difference between the voltage defined by the Tafel slope and the voltage derived by I-V (IR-free) curves was regarded as the concentration overvoltage.[6,44]

The ECSA of the Pt-based cathode electrocatalyst layers was evaluated based on cyclic voltammograms. H_2 was supplied to the anode, and N_2 was supplied to the cathode. The Pt/C anode was used as a reference electrode, and the potential of the cathode was set to be 0.5 to 0.9 V_{RHE}. 50 potential cycles were first applied in order to clean the catalyst surface. After this, the N_2 flow was stopped, and the cyclic voltammograms were recorded between 0.05 and 0.9 V_{RHE}. The ECSA was obtained from the peak area in the hydrogen desorption region (0.05 - 0.4 V_{RHE}), following the standard NEDO protocols.[53]

To evaluate the durability of MEAs, accelerated degradation tests were also performed, similar to the half-cell durability tests. A protocol simulating the start-stop cycles of an FCV was used, as recommended by the FCCJ[43] and NEDO.[44] According to this protocol, the potential was varied in a triangular waveform between 1.0 and 1.5 V with 2 seconds per cycle. A protocol simulating load cycling of an FCV, as suggested by the FCCJ[43] and NEDO,[44] was also used. Here, the potential was varied in a rectangular waveform between 0.6 and 1.0 V, with 6 seconds per cycle.

Results and Discussion

Microstructure of electrocatalysts: FE-SEM analysis.—Figure 2a, 2b shows FE-SEM images of the Nb-SnO_2/VGCF support. It is observed that SnO_2 particles with a diameter of ~10 to 20 nm are homogeneously decorated on the surface of the VGCF filler. The mass ratio of Nb-SnO_2 was 49.1 wt%, measured by TG, confirming that the final Nb-SnO_2/VGCF ratio was close to that expected from the selected precursor ratio. Figure 2c, 2d shows FE-SEM images of Pt_3Co/Nb-SnO_2/VGCF, after electrocatalyst decoration. Pt/Co nanoparticles with a diameter of 2 to 3 nm are selectively impregnated on the SnO_2 surface, rather than on the VGCF surface. Selective decoration of Pt-based catalyst particles is clearly seen especially in Fig. 2d. Pt-based catalyst particles of a few nanometers in diameter with bright contrast are deposited on the SnO_2 grains of a few tens of nanometers, rather than on the relatively-flat surface of the tubular VGCFs with dark contrast. From ICP-AES results, the atomic ratio of these nanoparticles was measured to be 74.2/25.8, corresponding to Pt_3Co.

Optimization of the preparation conditions.—Table I summarizes the different electrocatalysts subjected to half-cell measurements, showing the Pt:M atomic ratio, and the heat-treatment conditions after decoration with Co or Ni. In order to try and improve the catalytic activity, electrocatalysts were prepared with Pt:M ratios of 1:1, 3:1, and 4:1. The temperature of the second heat-treatment step is of critical importance. If the heat-treatment temperature after decoration of Co or Ni is too low, Pt-M alloying is not promoted. On the other hand, if the heat-treatment temperature is too high, SnO_2 can be reduced to metallic Sn, which has low melting point (231.9°C). This promotes Pt-Sn alloying rather than Pt-M alloying, leading to lower electrochemical activity.[14] We determined an optimized heat-treatment temperature to be 270°C, at which Pt-M alloying was promoted without reducing SnO_2 to metallic Sn.

Catalytic activity and start-stop cycle durability of electrocatalysts.—Figure 3 shows CVs and LSVs of the various Pt_xM_y/Nb-SnO_2/VGCF electrocatalysts (before cycling tests). Figure 3a shows that only minor differences can be seen in the hydrogen desorption region, regardless of the Pt:M ratio and the heat-treatment conditions. Figure 3b shows that the highest ORR activity is observed for Pt_3Co/Nb-SnO_2/VGCF (electrocatalyst #2), which has the most positively shifted LSV.

Figure 4 shows the change in ECSA over 60,000 start-stop potential cycles. Conventional Pt/C has the highest initial ECSA, but after 60,000 cycles this drops to 32% of the initial value. Pt/Nb-SnO_2/VGCF is the most durable, with ca. 70% ECSA retention after 60,000 cycles. Pt_3Co/Nb-SnO_2/VGCF (electrocatalyst #2) has an ECSA retention of 54% after 60,000 cycles. This is much higher than Pt/C, and this is attributed to selective decoration of the Pt_3Co nanoparticles on the Nb-SnO_2 support, meaning that they are not in direct contact with the carbon fibers (as observed in Figure 2), thus preventing carbon corrosion. However, the durability is not as good

Table I. Pt_xM_y electrocatalysts prepared with various atomic ratios of Pt:M and different heat-treatment conditions.

	Sample	Pt:M (at.%)	Heat-treatment conditions after the impregnation of M
#1	PtCo/Nb-SnO_2/VGCF	49.3:50.7	210°C (3 h) → 240°C (3 h) → 270°C (1 h)
#2	Pt_3Co/Nb-SnO_2/VGCF	74.2:25.8	210°C (3 h) → 240°C (3 h) → 270°C (1 h)
#3	Pt_4Co/Nb-SnO_2/VGCF	82.6:17.4	210°C (3 h) → 240°C (3 h) → 270°C (1 h)
#4	Pt_3Ni/Nb-SnO_2/VGCF	75.2:24.8	210°C (3 h) → 240°C (3 h) → 270°C (1 h)
#5	Pt_3Co/Nb-SnO_2/VGCF	74.6:25.4	240°C (3 h) → 270°C (3 h)

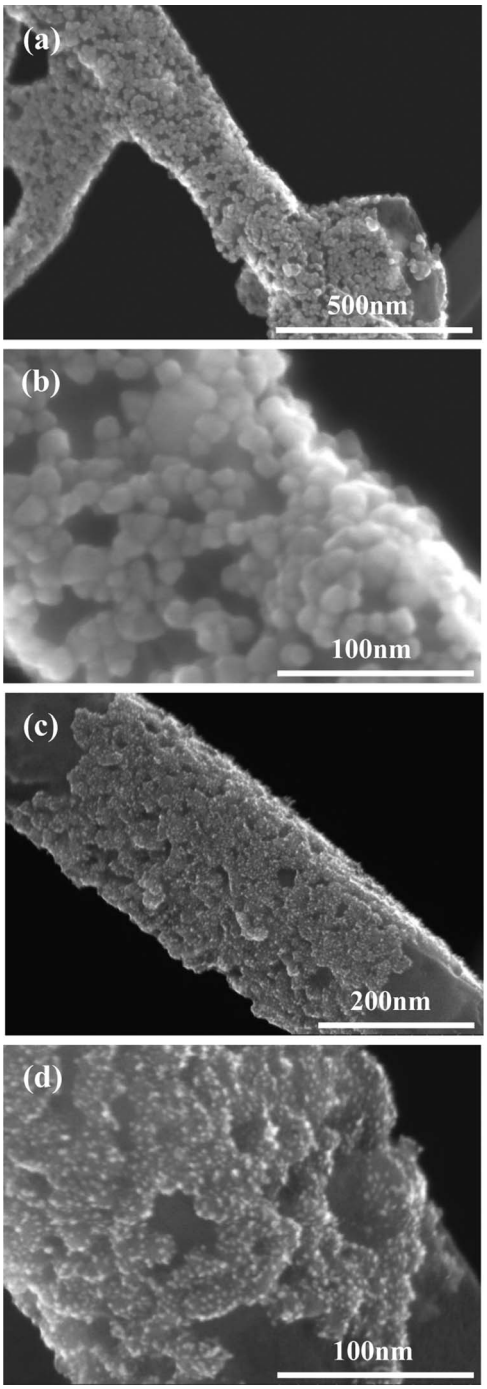

Figure 2. FE-SEM images of (a,b) Nb-SnO_2/VGCF and (c,d) Pt_3Co/Nb-SnO_2/VGCF electrocatalysts, with (a,c) lower magnification and (b,d) higher magnification.

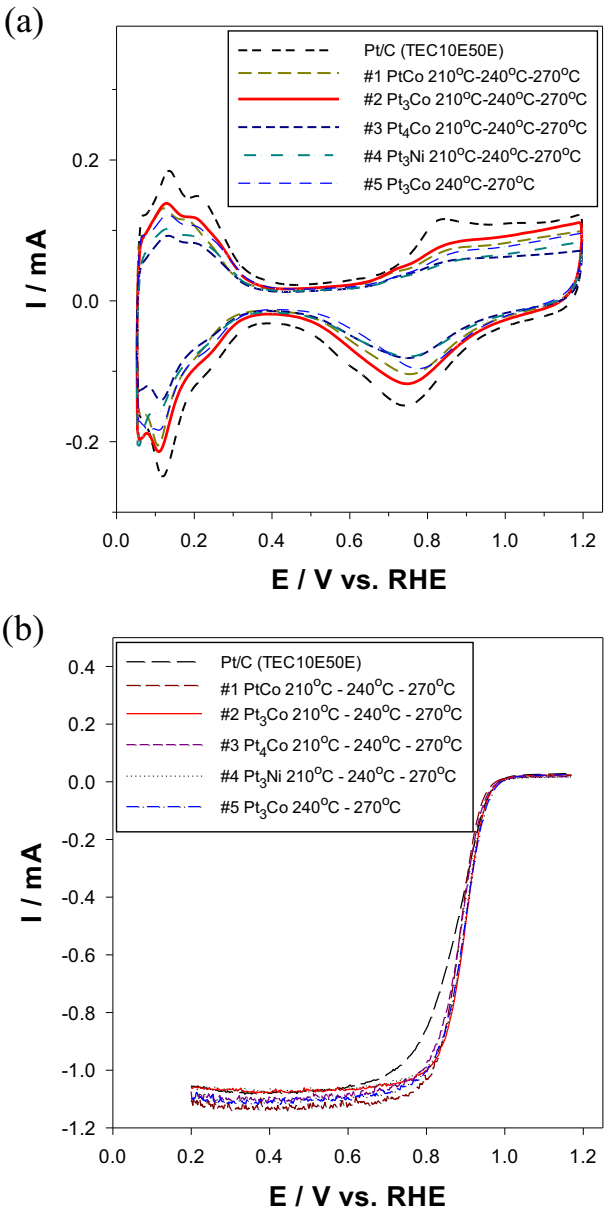

Figure 3. (a) Cyclic voltammograms of each electrocatalyst, measured in N_2-saturated 0.1 M $HClO_4$, at 25°C and 50 mV s^{-1}. (b) Linear sweep voltammograms (LSV) of each electrocatalyst, measured in O_2-saturated 0.1 M $HClO_4$, at 25°C and 10 mV s^{-1} at 1600 rpm.

as mono-metallic Pt/Nb-SnO_2/VGCF. The reasons for this will be discussed later with the aid of high-resolution STEM observations.

Figure 5 shows the mass activity (j_m) measured at 0.9 V_{RHE}, before and after start-stop potential cycling. This clearly shows that the initial ORR activity was improved by Pt_xM_y alloying, with the mass activity of all bimetallic electrocatalysts exceeding that of Pt/Nb-SnO_2/VGCF.

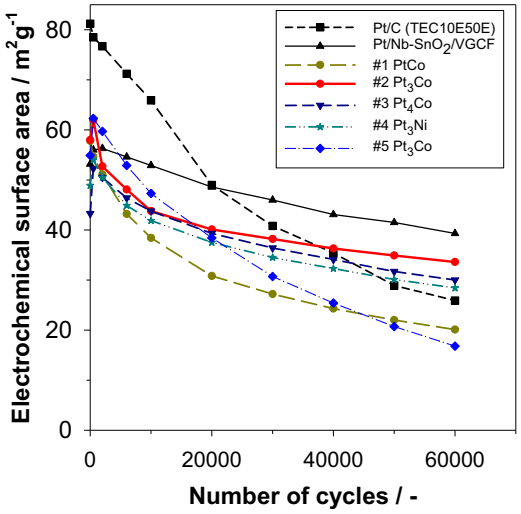

Figure 4. Change in ECSA of Pt and Pt_xM_y electrocatalysts as a function of the number of start-stop potential cycles.

The highest initial mass activity, 274 A g^{-1} at 0.9 V_{RHE} and 1840 A g^{-1} at 0.85 V_{RHE}, is observed for Pt_3Co/Nb-SnO_2/VGCF (electrocatalyst #2), which was heat-treated at 210, 240, and 270°C. In addition, this electrocatalyst still has the highest mass activity after 60,000 start-stop potential cycles (despite the lower ECSA), with a mass activity retention of 37%. This is significantly higher than that of Pt/C (27%). However, the highest mass activity retention (53%) was observed for Pt/Nb-SnO_2/VGCF. The ECSA and mass activity values of selected electrocatalysts before and after start-stop durability tests at 0.9 V_{RHE} and at 0.85 V_{RHE} (except for Pt/C) are compiled in Table II.

Load cycle durability of electrocatalysts.—Load cycling durability tests were carried out over 400,000 potential cycles for Pt/C, Pt/Nb-SnO_2/VGCF, and Pt_3Co/Nb-SnO_2/VGCF (electrocatalyst #2, which had the highest ORR activity). Figure 6a shows CVs of Pt_3Co/Nb-SnO_2/VGCF during potential cycling, whilst Figure 6b shows the changes in ECSA. After 400,000 cycles, the degradation was serious, and therefore the kinetic current could not be derived from the Koutecky-Levich plots. Therefore, Figure 7 compares the LSVs before and after the load potential cycling to show the changes in ORR activity.

Figure 6b shows that ECSA fell to 50% of the initial value after only ~40,000 cycles in case of the Pt/C. On the other hand, for Pt/Nb-SnO_2/VGCF, 50% degradation is observed after ~200,000 cycles. In the case of Pt_3Co/Nb-SnO_2/VGCF, 50% degradation is observed after ~60,000 cycles. After the full 400,000 cycles, 29.8% of the initial ECSA is retained in the case of Pt_3Co/Nb-SnO_2/VGCF, which is similar to the case of Pt/Nb-SnO_2/VGCF (30.3%), and much larger than that of Pt/C (14.9%). In the LSVs shown in Figure 7, it can be seen that Pt_3Co/Nb-SnO_2/VGCF exhibits a smaller negative shift in the oxygen reduction potential after load cycling, compared with Pt/C.

These results indicate that the Pt_3Co alloy electrocatalyst supported on Nb-SnO_2 exhibits higher load cycle durability compared with the conventional Pt/C electrocatalyst, in terms of both ECSA and ORR. Whilst the degradation associated with dissolution of Co from the bimetallic Pt-Co nanoparticles is expected to be more severe in load cycling tests, in this case we expect that the high binding energy between Pt and SnO_2 will suppress platinum mobility and dissolution.[54] Whilst Pt dissolution may be influenced by interactions with the catalyst support, as reported e.g. for nitrogen-modified carbon supports,[55,56] the possible influence on the dissolution of Pt and alloyed metals will be an important subject of future studies. Herein, we perform microstructural evaluation in order to gain more insight into the degradation processes.

Microstructure of electrocatalysts before and after durability tests: STEM analysis.—In order to analyze degradation phenomena in the Pt_3Co/Nb-SnO_2/VGCF electrocatalysts, the microstructure before and after durability tests was observed using STEM-EDS. The Pt-Co alloy was also analyzed by XRD, but the diffraction peaks of SnO_2 were too strong, making it difficult to distinguish the signals from Pt_3Co. Figure 8 shows EDS mapping of Nb-SnO_2/VGCF before Pt-decoration. The distribution of Sn and Nb elements is identical, indicating homogeneous Nb-doping of SnO_2. This may be attributed to e.g. intensive homogenization of the precipitates and an optimized

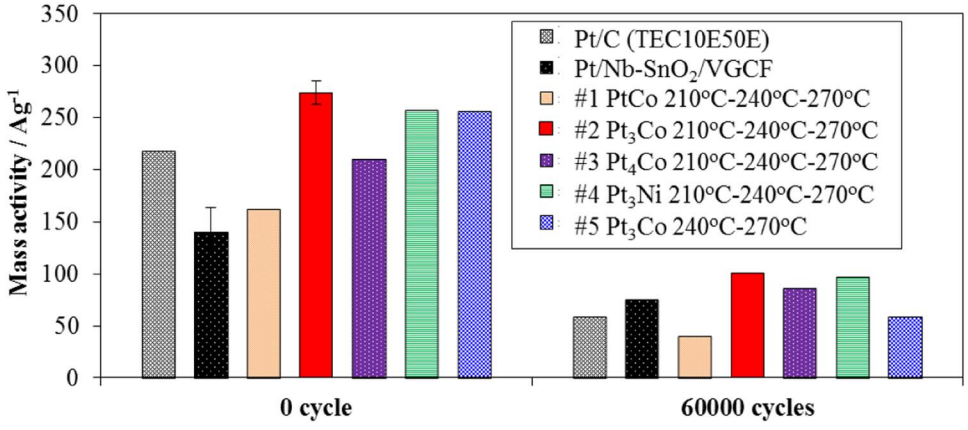

Figure 5. Mass activity (j_m) at 0.9 V_{RHE}, measured before (0 cycle) and after 60,000 start-stop potential cycles.

Table II. ECSA and mass activity before and after start-stop durability tests.

Sample	ECSA [m^2/g] (0 cycle)	Mass Activity [A/g] (0 cycle) @0.9 V_{RHE}	Mass Activity [A/g] (0 cycle) @0.85 V_{RHE}	Mass Activity [A/g] (after 60,000 cycles) @0.9 V_{RHE}	Mass Activity [A/g] (after 60,000 cycles) @0.85 V_{RHE}
Pt/C (TEC10E50E)	81.2	218	-	58.2	-
Pt/Nb-SnO_2/VGCF	51.1	141	541	75.0	289
Pt_3Co/Nb-SnO_2/VGCF	61.5	274	1,840	101	439

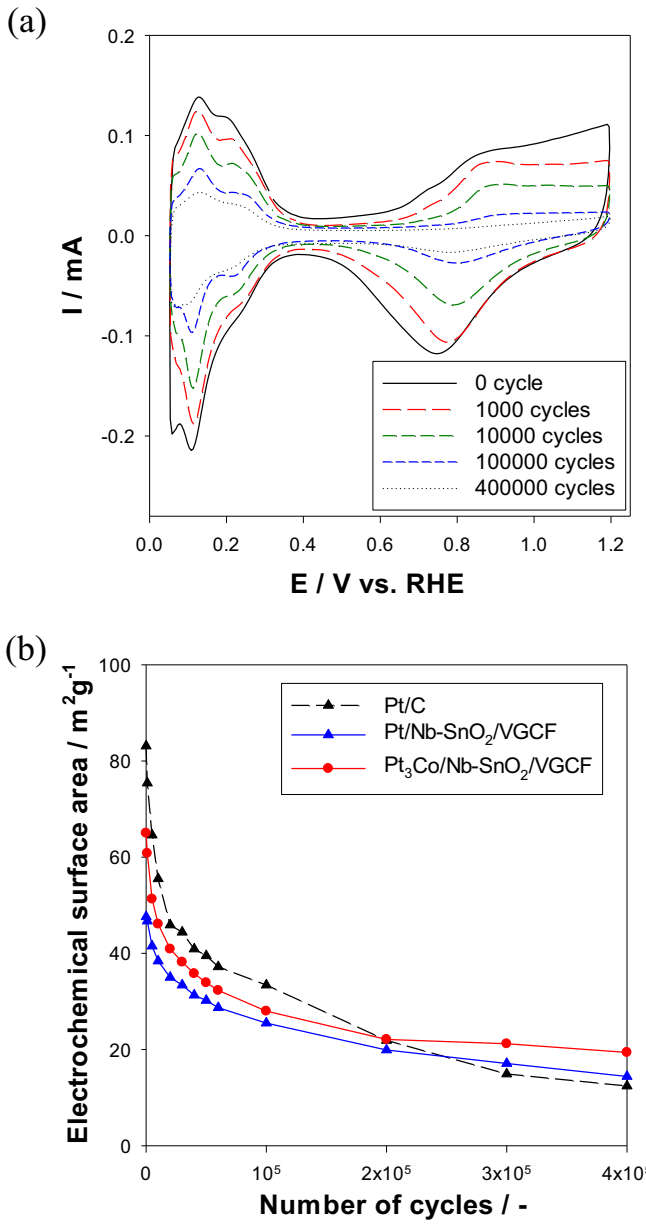

Figure 6. (a) Change in the CVs of Pt_3Co/Nb-SnO_2/VGCF (electrocatalyst #2) up to 400,000 load potential cycles, measured in N_2-saturated 0.1 M $HClO_4$ at 25°C and 50 mV s^{-1}. (b) Change in the ECSA of each electrocatalyst under the same conditions.

heat-treatment in the ammonia co-precipitation process, widely used in preparing various oxides such as SnO_2.[57,58] Figures 9 and 10 show Pt_3Co/Nb-SnO_2/VGCF electrocatalyst (#2) before and after 60,000 start-stop potential cycles, respectively. Figure 9 shows that catalyst nanoparticles with a size of ~2 to 3 nm are homogeneously dispersed on the SnO_2 support. The distribution of Pt in Fig. 9b and Co in Fig. 9d is almost identical, suggesting homogeneous alloying of Pt and Co. This EDS analysis also revealed a Pt:Co ratio of 3.6:1 before start-stop potential cycling. Figure 10a shows aggregation of Pt-based catalyst nanoparticles now connected with each other after 60,000 start-stop potential cycles. While the Co distribution in Fig. 10d is still similar to the Pt distribution in Fig. 10b, the Co signal became much weaker, with a Pt:Co ratio of 8.33:1 after 60,000 start-stop potential cycles.

Figure 11 shows STEM high-angle annular dark field (HAADF) images and EDS line profiles for Pt and Co distribution. Line profiles in Figure 11a confirm that the distribution of Co coincides with the distribution of Pt. Quantitative analysis of the EDS results con-

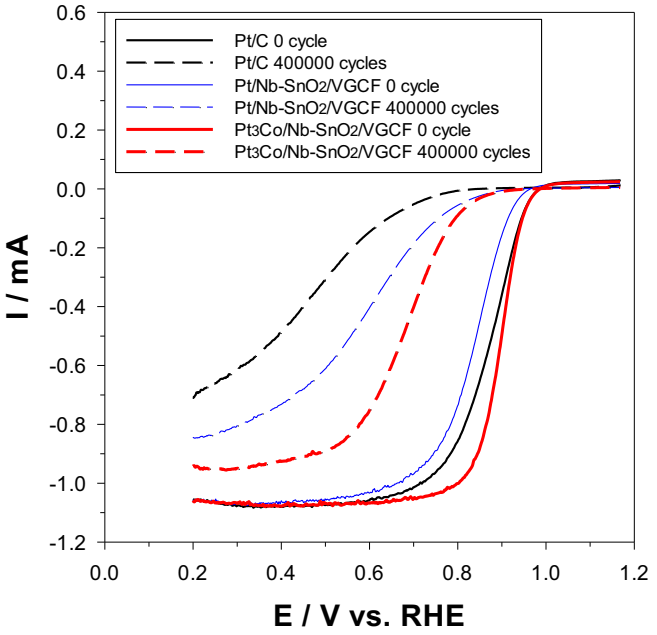

Figure 7. Comparison of LSVs of each electrocatalyst before and after 400,000 load potential cycles, measured in O_2-saturated 0.1 M $HClO_4$ at 25°C and 10 mV s^{-1}, at 1,600 rpm.

firms that the atomic ratio is ~3:1, corresponding to Pt_3Co. After start-stop potential cycling (Figure 11b), the STEM-EDS map shows that the Pt_3Co nanoparticles have increased in size to ~5 nm. In addition, the Pt/Co ratio increases significantly from ~3:1 to ~9:1 after the start-stop cycling test, and the intensity of the Co peaks in the line profile decreases. From these results, it is suggested that bimetallic Pt_3Co/Nb-SnO_2/VGCF degrades more significantly than Pt/Nb-SnO_2/VGCF, due to partial dissolution of the Co ions.

After applying 400,000 load potential cycles, the nanoparticle diameter is also observed to increase to ~10 nm (Figure 11c). The Pt/Co

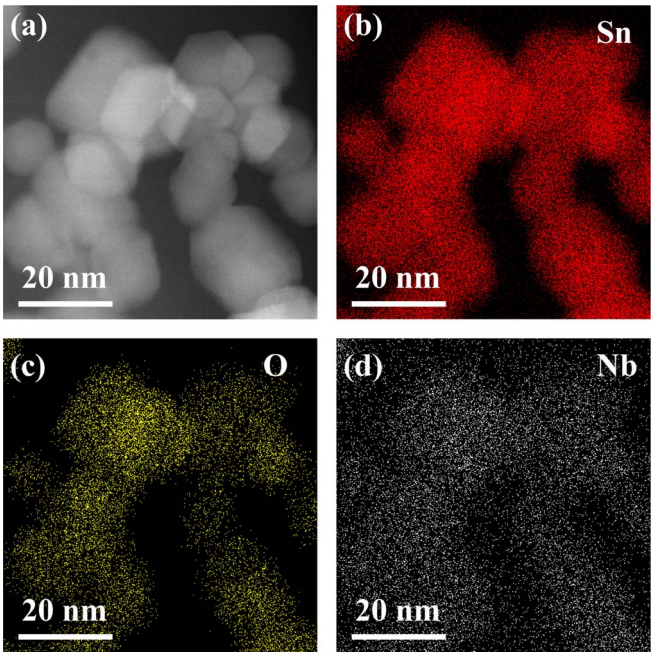

Figure 8. (a) STEM micrograph and EDS elemental maps of (b) Sn, (c) O, and (d) Nb, for Nb-SnO_2/VGCF before Pt-decoration.

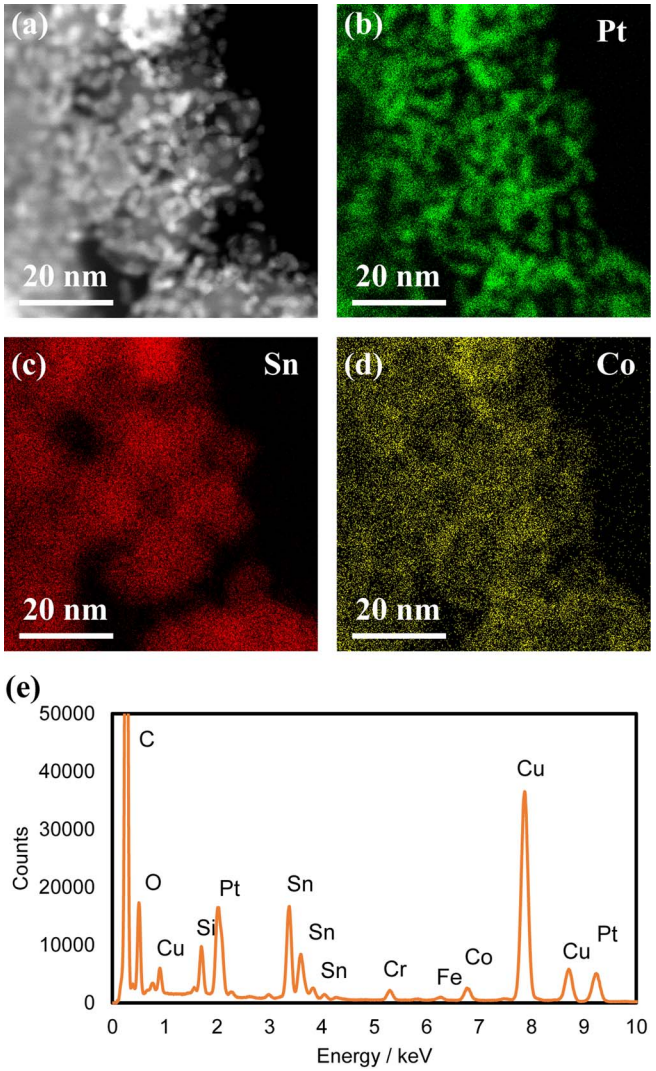

Figure 9. (a) STEM micrograph and EDS elemental maps of (b) Pt, (c) Sn, and (d) Co, of the Pt_3Co/Nb-SnO_2/VGCF electrocatalyst (#2) *before* 60,000 start-stop potential cycles. EDS spectra are also shown in (e), while signals of foreign elements such as Cu, C, O, Si, Cr, and Fe originate from the Cu mesh, electron microscope components, and/or contaminants.

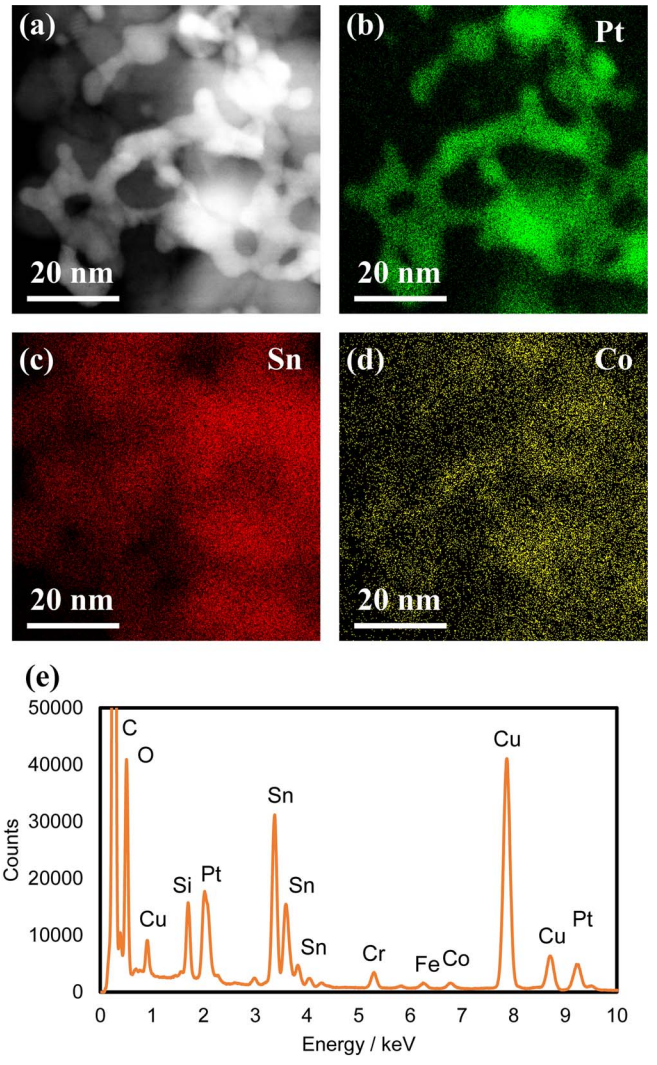

Figure 10. (a) STEM micrograph and EDS elemental maps of (b) Pt, (c) Sn, and (d) Co, of the Pt_3Co/Nb-SnO_2/VGCF electrocatalyst (#2) *after* 60,000 start-stop potential cycles. EDS spectra are also shown in (e), while signals of foreign elements such as Cu, C, O, Si, Cr, and Fe originate from the Cu mesh, electron microscope components, and/or contaminants.

ratio increases to ~9.6:1, similar to the case of start-stop cycling, indicating dissolution of Co. The line profile also clearly indicates a decrease in the Co concentration of the catalyst nanoparticles. This degradation during load cycling is attributed to dissolution of Co from the Pt-Co catalysts.

I-V performance and start-stop cycle durability of MEAs.—Initial I-V performance and start-stop cycle durability tests for MEAs fabricated with Pt_3Co/Nb-SnO_2/VGCF cathode electrocatalysts were investigated. Figure 12 shows (a) I-V characteristics, (b) overvoltages separated, (c) changes in cell voltage (at 0.2 A cm^{-2}) during start-stop durability tests, and (d) changes in the ECSA under the same conditions. The data on Pt/C and Pt/Nb-SnO_2/VGCF in Figures 12c and 12d is cited from Part I of this study.[6] Figure 12a shows a gradual degradation of the I-V characteristics during start-stop operation. Figure 12b indicates that this degradation is associated with a gradual increase in the activation overvoltage and the concentration overvoltage. Figure 12c confirms that the initial I-V performance of the MEA containing Pt_3Co/Nb-SnO_2/VGCF is comparable to that of the conventional Pt/C, despite the fact that the conditions of acid treatment, Nafion ratio, and the humidification temperature have not yet been optimized. After start-stop cycle operation, 94% of the initial cell voltage is retained for Pt_3Co/Nb-SnO_2/VGCF, which is much higher than that of Pt/C, and slightly higher than Pt/Nb-SnO_2/VGCF. This suggests that carbon corrosion is suppressed in these electrocatalysts, due to selective decoration of platinum on the Nb-SnO_2 rather than on the VGCF (see Figure 2). Figure 12d shows the change in ECSA of the MEAs. The initial value is 42.6 m^2 g^{-1}, which is ~1.4 times higher than that of Pt/Nb-SnO_2/VGCF. The slight increase in ECSA during the first few thousand cycles may be due to Co-dissolution near the catalyst surface, and the subsequent formation of a Pt skin at the top surface. In terms of start-stop cycle durability, 93% of the initial ECSA is retained after 60,000 cycles, similar to the case of Pt/Nb-SnO_2/VGCF. After around 2,000 cycles, the ECSA of the MEA made with Pt_3Co/Nb-SnO_2/VGCF is higher than that of the conventional Pt/C. As shown in Figure 12b, the activation overvoltage does not change, suggesting that Pt particles are highly stable on the Nb-SnO_2 support during the start-stop durability tests. This result is consistent with the stable ECSA in Figure 12d.

Load cycle durability of MEAs.—Load potential cycle durability tests up to 400,000 cycles were carried out for an MEA containing Pt_3Co/Nb-SnO_2/VGCF electrocatalyst, as shown in Figure 13. The

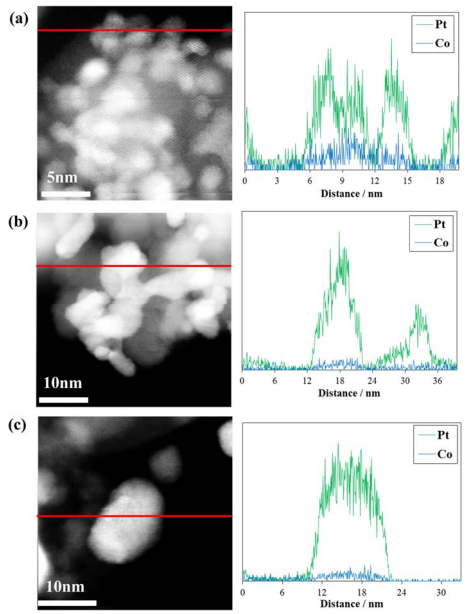

Figure 11. STEM-EDS HAADF images (left) and Pt and Co line profiles (along the red lines) for $Pt_3Co/Nb\text{-}SnO_2/VGCF$ (electrocatalyst #2): (a) before durability tests; (b) after 60,000 start-stop potential cycles; and (c) after 400,000 load potential cycles. The elemental distribution of Pt and Co along the red line is shown in each figure on the right side.

data on Pt/C and $Pt/Nb\text{-}SnO_2/VGCF$ in Figures 13c and 13d is cited from the Part I of this study.[6] Figure 13a reveals significant degradation of the I-V characteristics during load cycle testing. Figure 13b indicates that this is mainly due to a clear increase in the activation overvoltage, and partly due to a small increase in the concentration overvoltage. The IR losses did not significantly change. Figure 13c shows that the initial cell voltage of the conventional Pt/C is high, but that the degradation rate is also high. Meanwhile the cell voltage degradation of $Pt_3Co/Nb\text{-}SnO_2/VGCF$ is much slower, leading to higher cell voltage than Pt/C after the 400,000-cycle durability test. Figure 13d shows that the ECSA of the $Pt_3Co/Nb\text{-}SnO_2/VGCF$ MEA decreases up to 100,000 load cycles. This degradation is faster than in the case of the $Pt/Nb\text{-}SnO_2/VGCF$ MEA, which is attributed to dissolution of Co. Meanwhile this degradation rate is much higher in the conventional Pt/C.

Microstructure of the MEAs before and after durability tests: STEM analysis.—The microstructure of the MEA electrocatalysts was observed by high-resolution STEM-EDS. Figure 14 shows HAADF images and EDS line profiles before and after each durability test. The line profiles confirm that the distribution of Co coincides with that of Pt in the $Pt_3Co/Nb\text{-}SnO_2/VGCF$ electrocatalyst, before durability tests. However, the Pt:Co ratio quantitatively calculated from the EDS results is ~19:1, which is much lower than that calculated from ICP-AES. In this sample, the heat-treatment temperature was relatively low (270°C) in order to prevent the reduction of SnO_2 to Sn metal. This may have resulted in incomplete reduction of $Co(acac)_2$, the remainder of which would be lost during the acid washing step before MEA preparation, contributing to the lower Co content seen here.

After both the start-stop and load cycling tests, it can be seen that the diameter of the Pt-Co nanoparticles increases from ~5 nm to ~10 nm (Figures 14b and 14c). The Pt:Co ratio was 17.5:1 after the start-stop test, and 22:1 after the load cycle test, indicating negligible change within error during the start-stop and load cycling tests. This is attributed to the fact that in the case of an MEA, the dissolved Co stays inside the electrocatalyst layer, unlike the case of half-cell measurements, in which the Co is lost to the electrolyte solution.

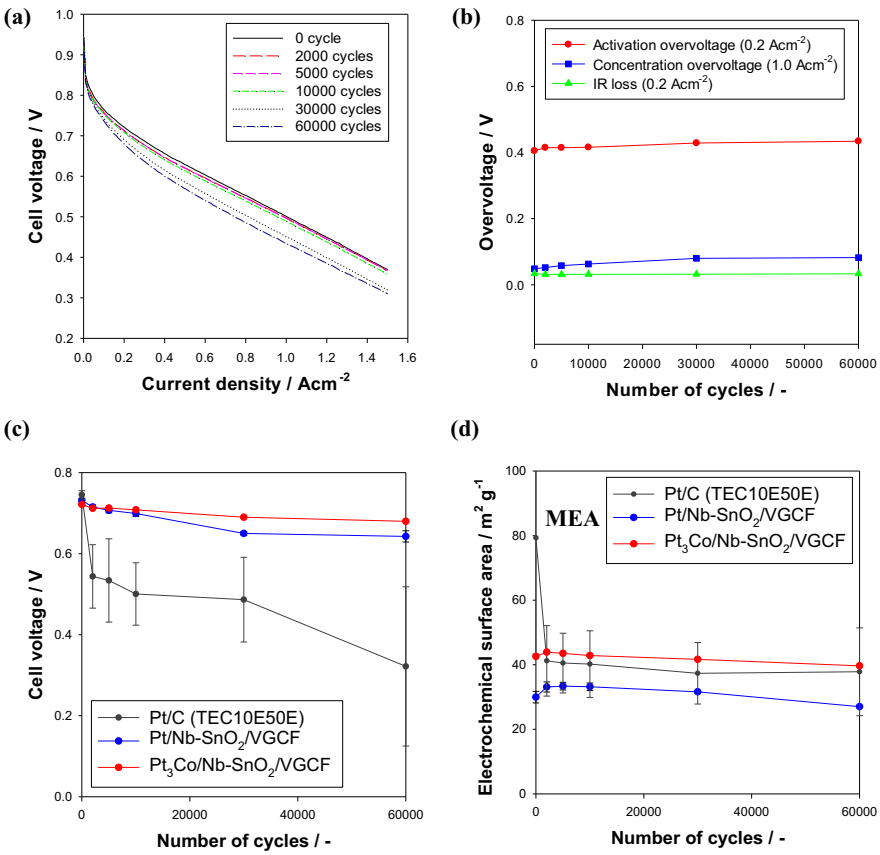

Figure 12. MEA performance over 60,000 start-stop potential cycles. (a) I-V characteristics, and (b) overvoltage separation for $Pt_3Co/Nb\text{-}SnO_2/VGCF$. (c) Changes in cell voltage at 0.2 A cm^{-2}, and (d) changes in ECSA of MEAs containing $Pt_3Co/Nb\text{-}SnO_2/VGCF$, $Pt/Nb\text{-}SnO_2/VGCF$, and Pt/C.

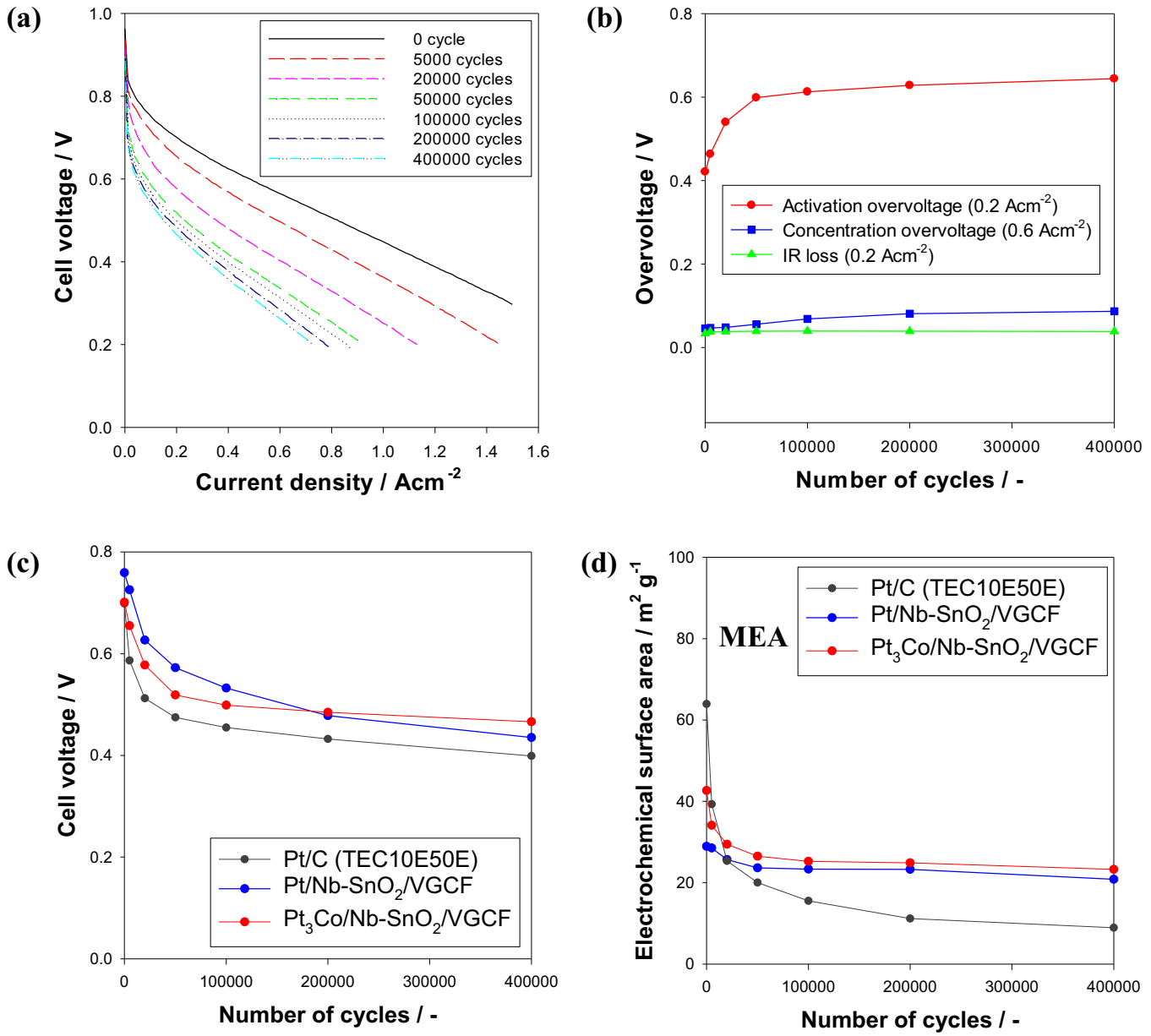

Figure 13. MEA performance over 400,000 load potential cycles. (a) I-V characteristics, and (b) overvoltage separation for $Pt_3Co/Nb\text{-}SnO_2/VGCF$. (c) Changes in cell voltage at 0.2 A cm^{-2}, and (d) changes in ECSA of MEAs containing $Pt_3Co/Nb\text{-}SnO_2/VGCF$, $Pt/Nb\text{-}SnO_2/VGCF$, and Pt/C.

Figure 15 shows cross-sectional STEM-HAADF images of the MEA cathode electrocatalyst layers after 400,000 load cycles, highlighting heavy elements like Pt and Sn with brighter contrast. Sliced thin specimens with a thickness of <100 nm for STEM observation were prepared by focused ion beam (FIB). In general, HAADF-STEM signals scale strongly with the atomic number. Therefore, Pt catalysts have a brighter contrast within the Pt/C cathode layer in Figure 15a, and Pt and SnO_2 particles exist as brighter parts in Figures 15b and 15c. The electrolyte membrane is located on the bottom side of the image, and the carbon paper was on the top (this was removed before the FIB processing). After 400,000 load cycle tests, the Pt/C electrocatalyst layer became more dense and much thinner (Figure 15a), while the oxide-supported electrocatalyst layers retained high porosity (Figures 15b and 15c). For Pt/C (Figure 15a), a Pt-rich (brighter) layer with a thickness of 1 to 2 μm is observed at the cathode/electrolyte interface after the load cycle test, which was also verified by EDS analysis. In contrast, for $Pt/Nb\text{-}SnO_2/VGCF$ (Figure 15b) and $Pt_3Co/Nb\text{-}SnO_2/VGCF$ (Figure 15c), the catalyst nanoparticles (brighter in the image) are still homogeneously distributed throughout the electrocatalyst layers. In addition, no Pt-rich layer was observed near the cathode/electrolyte interface. This explains the high load cycle durability of oxide-supported MEAs.

Figure 16 shows STEM-HAADF images of the electrocatalysts in the MEAs after 400,000 load cycles. Figure 16a shows clear growth of the Pt catalyst particles after this load cycle test for the Pt/C electrocatalyst. Further aggregation of the Pt particles can be observed in Figure 16b, near the cathode/membrane interface, forming the Pt-rich layer shown in Figure 15a. In contrast, Figure 16c clearly shows Pt-based nanoparticles of several nm in diameter (with bright contrast), still well-dispersed on the SnO_2-based support (with a diameter of a few tens of nm, gray contrast) in the $Pt_3Co/Nb\text{-}SnO_2/VGCF$ cathode, after the load cycle durability test. A similar dispersion of Pt-based catalyst nanoparticles also remains near the cathode/membrane interface, as shown in Figure 16d. These results clearly indicate the microstructural stability of the $Pt_3Co/Nb\text{-}SnO_2/VGCF$ cathode layer against severe load potential cycles.

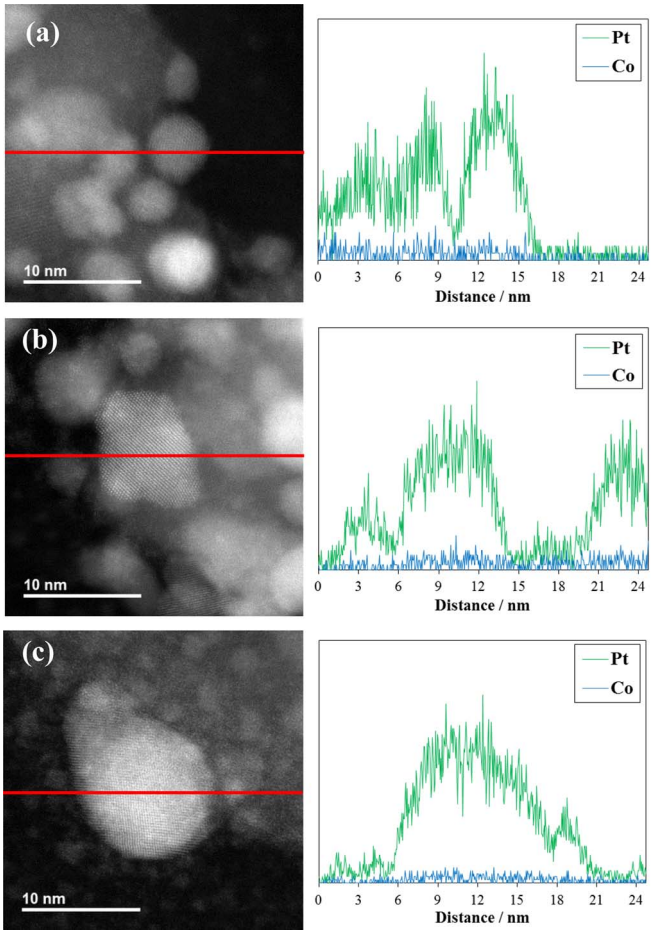

Figure 14. STEM-EDS HAADF images and Pt and Co line profiles (along the red lines) for MEAs with $Pt_3Co/Nb\text{-}SnO_2/VGCF$: (a) before durability tests; (b) after 60,000 start-stop potential cycles; and (c) after 400,000 load potential cycles. The elemental distribution of Pt and Co along the red line is shown in each figure on the right side.

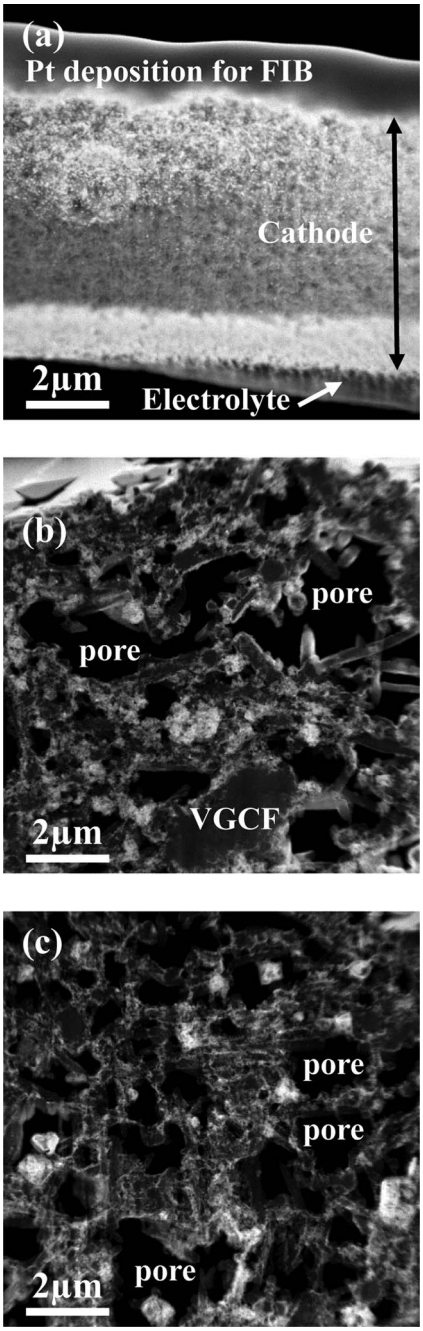

Figure 15. STEM HAADF cross-sectional images of the MEA cathode electrocatalyst layer after 400,000 load potential cycles: (a) Pt/C; (b) $Pt/Nb\text{-}SnO_2/VGCF$; and (c) $Pt_3Co/Nb\text{-}SnO_2/VGCF$.

The experimental verification of the high stability of oxide-supported electrocatalysts against load potential cycling is of significant scientific and technological interest. Load potential cycles are typically associated with the dissolution of Pt (and alloyed metals).[43,56,59,60] Therefore the interaction between the Pt and the oxide support is expected to affect the degradation phenomena associated with load cycling. In this case, the enhanced durability is likely to be related to the higher binding energy between platinum and SnO_2, compared with that between platinum and carbon in Pt/C.[54] Higher binding energy is expected to suppress the mobility of platinum as well as platinum aggregation compared to the case of Pt/C, and may also suppress dissolution-related phenomena. Detailed mechanisms for this should be clarified in future studies. Quantitative EDS analysis of the Pt:Co ratio of $Pt_3Co/Nb\text{-}SnO_2/VGCF$ from Figure 15c gives a Pt:Co ratio of ~15:1 near the carbon paper, and ~13:1 near the electrolyte membrane, which are the same within error. This means that the dissolved Co still remains within the MEA electrocatalyst layer, contributing also to the high load cycle durability.

Figure 17 shows the particle size distribution for the different Pt-alloy catalysts before voltage cycling, after 60,000 start-stop cycles, and after 400,000 load cycles, corresponding to the lifetime of an FCV. While some degradation associated with catalyst particle growth was observed, these results also confirm sufficient durability and lifetime of the developed Pt-alloy SnO_2-supported electrocatalysts under realistic PEFC operating conditions.

Conclusions

Pt_xM_y alloy bimetallic catalysts decorated on SnO_2-based supports with conductive VGCF carbon fillers were prepared, leading to improvements in the catalytic activity. A high mass activity of 274 A g^{-1} at 0.9 V_{RHE} and 1840 A g^{-1} at 0.85 V_{RHE} was achieved. The initial I-V performance of MEA with the $Pt_3Co/Nb\text{-}SnO_2/VGCF$ electrocatalyst layer was similar to that of the conventional Pt/C electrocatalyst. Bimetallic $Pt_3Co/Nb\text{-}SnO_2/VGCF$ electrocatalysts displayed excellent start-stop cycle durability and high load cycle durability in both half-cell and full-cell MEA configuration. These results show that bimetallic Pt-alloy electrocatalysts on oxide supports with a conductive carbon backbone can simultaneously achieve high initial ORR

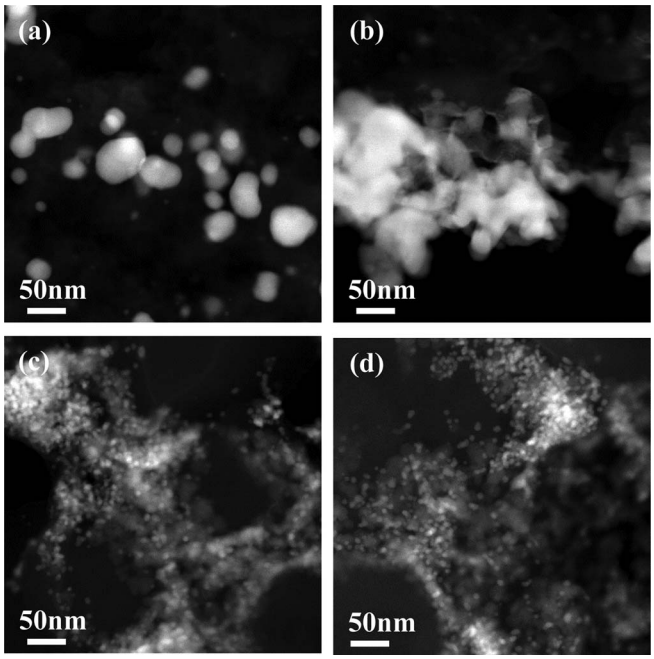

Figure 16. STEM-HAADF images of the electrocatalysts in the MEAs after 400,000 load cycles; (a), (b) Pt/C; and (c), (d) Pt_3Co/Nb-SnO_2/VGCF. (a) and (c) were taken from the cathode layer near the carbon paper, while (b) and (d) from the cathode layer near the cathode/membrane interface.

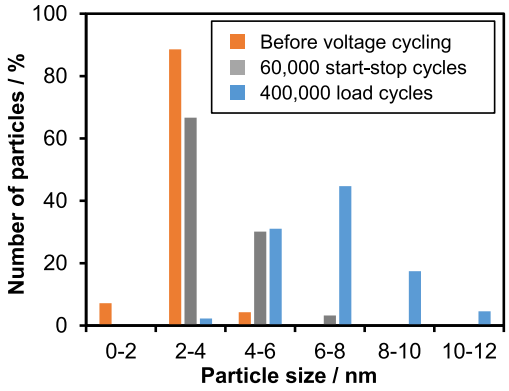

Figure 17. Particle size distribution of the Pt_3Co/Nb-SnO_2/VGCF electrocatalyst before voltage cycling, after the 60,000 start-stop cycles, and after the 400,000 load cycles.

activity, cell voltage, start-stop cycle durability, and load cycle durability.

Acknowledgments

Financial support by the Center-of-Innovation (COI) program, JST Japan, is gratefully acknowledged.

ORCID

K. Sasaki https://orcid.org/0000-0002-3174-9087

References

1. Y. Tanaka, Development of the MIRAI Fuel Cell Vehicle, Chapter 34 in *Hydrogen Energy Engineering: A Japanese Perspective*, Ed. by K. Sasaki, H.-W. Li, A. Hayashi, J. Yamabe, T. Ogura, and S. M. Lyth, Springer Japan, (2016).
2. J. Larminie and A. Dicks, *Fuel Cell Systems Explained*, 2nd ed., JohnWiley & Sons, England (2003).
3. L. M. Roen, C. H. Paik, and T. D. Jarvi, *Electrochem. Solid-State Lett.*, **7**(1), A19 (2004).
4. A. Taniguchi, T. Akita, K. Yasuda, and Y. Miyazaki, *J. Power Sources*, **130**(1-2), 42 (2004).
5. C. A. Reiser, L. Bregoli, T. W. Patterson, J. S. Yi, D. Yang, M. L. Perry, and T. D. Jarvi, *Electrochem. Solid-State Lett.*, **8**(6), A273 (2005).
6. Y. Nakazato, D. Kawachino, Z. Noda, J. Matsuda, S. M. Lyth, A. Hayashi, and K. Sasaki, *J. Electrochem. Soc.*, **165**, 1154 (2018).
7. X. Wang, W. Z. Li, Z. W. Chen, M. Waje, and Y. S. Yan, *J. Power Sources*, **158**(1), 154 (2006).
8. X. Zhao, A. Hayashi, Z. Noda, K. I. Kimijima, I. Yagi, and K. Sasaki, *Electrochim. Acta*, **97**, 33 (2013).
9. T. Ioroi, Z. Siroma, N. Fujiwara, S. Yamazaki, and K. Yasuda, *Electrochem. Comm.*, **7**(2), 183 (2005).
10. M. Nakada, A. Ishihara, S. Mitsushima, N. Kamiya, and K. Ota, *Electrochem. Solid-State Lett.*, **10**(1), F1 (2007).
11. B. L. Garcia, R. Fuentes, and J. W. Weider, *Electrochem. Solid-State Lett.*, **10**(7), B108 (2007).
12. K. S. Lee, I. S. Park, Y. H. Cho, D. S. Jung, N. Jung, H. Y. Park, and Y. E. Sung, *J. Catal.*, **258**(1), 143 (2008).
13. K. Sasaki, F. Takasaki, Z. Noda, S. Hayashi, Y. Shiratori, and K. Ito, *ECS Trans.*, **33**(1), 473 (2010).
14. A. Masao, S. Noda, F. Takasaki, K. Ito, and K. Sasaki, *Electrochem. Solid-State Lett.*, **12**(9), B119 (2009).
15. F. Takasaki, S. Matsuie, Y. Takabatake, Z. Noda, A. Hayashi, Y. Shiratori, K. Ito, and K. Sasaki, *J. Electrochem. Soc.*, **158**(10), B1270 (2011).
16. T. Kuroki, K. Sasaki, H. Kusaba, and Y. Teraoka, *206th ECS meeting abstract*, MA2004-02, #1527 (2004).
17. A. Masao, Z. Noda, F. Takasaki, K. Ito, and K. Sasaki, "Method for producing electrode material for fuel cell, electrode material for fuel cell, and fuel cell using the electrode material for fuel cell", WO 2009060582, *World Intellectual Property Organization*, Priority Data: 9.11.2007; International Filing Date: 31.10.2008.
18. T. Tsukatsune, Y. Takabatake, Z. Noda, T. Daio, A. Zaitsu, S. M. Lyth, A. Hayashi, and K. Sasaki, *J. Electrochem. Soc.*, **161**(12), F1208 (2014).
19. K. Kakinuma, M. Uchida, T. Kamino, H. Uchida, and M. Watanabe, *Electrochim. Acta*, **56**, 2881 (2011).
20. D. Horiguchi, T. Tsukatsune, Z. Noda, A. Hayashi, and K. Sasaki, *ECS Trans.*, **64**(3), 215 (2014).
21. T. Binninger, R. Mohamed, A. Patru, K. Waltar, E. Gericke, X. Tuaev, E. Fabbri, P. Levecque, A. Hoell, and T. J. Schmidt, *Chem. Mater.*, **29**(7), 2831 (2017).
22. Y. Takabatake, Z. Noda, S. M. Lyth, A. Hayashi, and K. Sasaki, *International J. Hydrogen Energy*, **39**(10), 5074 (2014).
23. E. Oakton, J. Tillier, G. Siddiqi, Z. Mickovic, O. Sereda, A. Fedorov, and C. Copéret, *New J. Chem.*, **40**(3), 2655 (2016).
24. A. S. Mukerjee and S. Srinivasan, *J. Electroanal. Chem.*, **357**(1-2), 201 (1993).
25. T. Toda, H. Igarashi, and M. Watanabe, *J. Electrochem. Soc.*, **145**(12), 4185 (1998).
26. T. Toda, H. Igarashi H. Uchida, and M. Watanabe, *J. Electrochem. Soc.*, **146**(10), 3750 (1999).
27. M. Oezaslan, F. Hasche, and P. Strasser, *J. Electrochem. Soc.*, **159**(4), B394 (2012).
28. M. Asano, R. Kawamura, N. Todoroki, and T. Wadayama, *ECS Trans.*, **75**(14), 809 (2016).
29. S. Kühl, H. Heyen, and P. Strasser, *ECS Trans.*, **75**(14) 723 (2016).
30. T. Tada, Y. Yamamoto, K. Matsutani, K. Hayakawa, and T. Namai, *ECS Trans.*, **16**(2), 215 (2008).
31. A. Stassi, I. Gatto, A. Patti, G. Monoforte, V. Baglio, and A. S. Arico, *ECS Trans.*, **69**(17), 263 (2015).
32. V. R. Stamenkovic, B. Fowler, B. S. Mun, G. Wang, P. N. Ross, C. A. Lucas, and N. M. Marković, *Science*, **315**(5811), 493 (2007).
33. J. Wu, J. Zhang, Z. Peng, S. Yang, F. T. Wagner, and H. Yang, *J. Am. Chem. Soc.*, **132**(14), 4984 (2010).
34. B. B. Han, C. E. Carlton, A. Kongkanand, R. S. Kukreja, B. R. Theobald, L. Gan, R. O'Malley, P. Strasser, F. T. Wagnerd, and Y. Shao-Horn, *Energy Environ. Sci.*, **8**(1), 258 (2015).
35. H. A. Gasteiger, S. S. Kocha, B. Sompalli, and F. T. Wagner, *Appl. Catalysis B: Environmental*, **56**(1-2), 9 (2005).
36. V. R. Stamenkovic, B. S. Mun, M. Arenz, K. J. J. Mayrhofer, C. A. Lucas, G. Wang, P. N. Ross, and N. M. Marković, *Nature Mater.*, **6**(3), 241 (2007).
37. D. Thompsett, Pt alloys as oxygen reduction catalysts, in *Handbook of Fuel Cells – Fundamentals, Technology and Applications*, Ed. by W. Vielstich, H. Gasteiger, A. Lamm, and H. Yokokawa, John Wiley & Sons, (2010).
38. M. K. Debe, *Nature*, **486**(7401), 43 (2012).
39. I. E. L. Stephens, J. Rossmeisl, and I. Chorkendorff, *Science*, **354**(6318), 1378 (2016).
40. S. Lankiang, M. Chiwata, S. Baranton, H. Uchida, and C. Coutanceaua, *Electrochim. Acta.* **182**, 131 (2015).
41. V. Kepeniene, R. Stagniunaite, L. Tamasauskaite, and E. Norkus, *ECS Trans.*, **69**(17), 643 (2015).
42. M. Ishida and K. Matsutani, *ECS Trans.*, **8**(8), 725 (2017).
43. A. Ohma, K. Shinohara, A. Iiyama, T. Yoshida, and A. Daimaru, *ECS Trans.*, **41**(1), 775 (2011).
44. New Energy and Industrial Technology Development Organization (NEDO), http://www.nedo.go.jp/content/100537904.pdf (accessed 2017-12-6).
45. H. R. Colón-Mercado, H. Kim, and B. N. Popov, *Electrochem. Comm.*, **6**(8), 795 (2004).
46. P. Yu, M. Pemberton, and P. Plasse, *J. Power Sources*, **144**(1), 11 (2005).

47. Y. Bing, H. Liu, L. Zhang, D. Ghosh, and J. Zhang, *Chem. Soc. Rev.*, **39**(6), 2184 (2010).
48. Showa Denko K. K., http://www.sdk.co.jp/english/products/126/132/2094.html (accessed 2018-3-21).
49. A. Hayashi, H. Notsu, K. Kimijima, J. Miyamoto, and I. Yagi, *Electrochim Acta*. **53**, 6117 (2008).
50. M. Inaba, H. Ito, H. Tuji, T. Wada, M. Banno, H. Yamada, M. Saito, and A. Tasaka, *ECS Trans*., **33**(1), 231 (2010).
51. P. Mani, R. Srivastava, and P. Strasser, *J. Power Sources*, **196**(2), 666 (2011).
52. M. Hori, K. Kobayashi, Y. Oono, and A. Daimaru, *ECS meeting abstract*, MA2012-02, #1497 (2012).
53. *Daido University, Ritsumeikan University*, Tokyo Institute of Technology, and Japan Automobile Research Institute, *Cell Evaluation and Analysis Protocol Guideline (Electrocatalyst, Support, Membrane and MEA)*, New Energy and Industrial Technology Development Organization (NEDO), Japan, (2014).
54. T. Daio, A. Staykov, L. Guo, J. Liu, M. Tanaka, S. M. Lyth, and K. Sasaki, *Sci. Rep.*, **5**, 13126 (2015).
55. Y. Zhou, K. Neyerlin, T. S. Olson, S. Pylypenko, J. Bult, H. N. Dinh, T. Gennett, Z. Shao, and R. O'Hayre, *Energy Environ. Sci.*, **3**(10), 1437 (2010).
56. J. Liu, T. Daio, K. Sasaki, and S. M. Lyth, *Fuel Cells*, **14**(5), 728 (2014).
57. K. Sasaki, H. P. Seifert, and L. J. Gauckler, *J. Electrochem. Soc.*, **141**(10), 2759 (1994).
58. K. Sasaki, *Phase equilibria, electrical conductivity, and electrochemical properties of ZrO_2-In_2O_3, PhD thesis*, Swiss Federal Institute of Technology (ETH-Zürich), Switzerland, 1993.
59. M. M. Mench, E. C Kumbur, and T. N. Veziroglu, *Polymer Electrolyte Fuel Cell Degradation*, Academic Press, Elsevier, 2012.
60. S. Mitsushima, S. Kawahara, K. Ota, and N. Kamiya, *J. Electrochem. Soc.*, **154**(2), B153 (2007).